Model selection for GRB 211211A through multi-wavelength analyses

Nina Kunert,[1] Sarah Antier,[2] Vsevolod Nedora,[3] Mattia Bulla,[4, 5, 6] Peter T. H. Pang,[7, 8] Shreya Anand,[9] Michael Coughlin,[10] Ingo Tews,[11] Jennifer Barnes,[12] Meili Pilloix,[2, 13] Weizmann Kiendrebeogo,[2] and Tim Dietrich[1, 3]

[1] *Institute of Physics and Astronomy, Theoretical Astrophysics, University Potsdam, Haus 28, Karl-Liebknecht-Str. 24/25, 14476, Potsdam, Germany*
[2] *Artemis, Observatoire de la Côte d'Azur, Université Côte d'Azur, Boulevard de l'Observatoire, 06304 Nice, France*
[3] *Max Planck Institute for Gravitational Physics (Albert Einstein Institute), Am Mühlenberg 1, Potsdam 14476, Germany*
[4] *Department of Physics and Earth Science, University of Ferrara, via Saragat 1, I-44122 Ferrara, Italy*
[5] *INFN, Sezione di Ferrara, via Saragat 1, I-44122 Ferrara, Italy*
[6] *INAF, Osservatorio Astronomico d'Abruzzo, via Mentore Maggini snc, 64100 Teramo, Italy*
[7] *Nikhef, Science Park 105, 1098 XG Amsterdam, The Netherlands*
[8] *Institute for Gravitational and Subatomic Physics (GRASP), Utrecht University, Princetonplein 1, 3584 CC Utrecht, The Netherlands*
[9] *Cahill Center for Astrophysics, California Institute of Technology, Pasadena CA 91125, USA*
[10] *School of Physics and Astronomy, University of Minnesota, Minneapolis, Minnesota 55455, USA*
[11] *Theoretical Division, Los Alamos National Laboratory, Los Alamos, NM 87545, USA*
[12] *Kavli Institute for Theoretical Physics, Kohn Hall, University of California, Santa Barbara, CA 93106, USA*
[13] *Laboratoire de Physique et de Chimie de l'Environnement, Université Joseph KI-ZERBO, Ouagadougou, Burkina Faso*

(Dated: January 6, 2023)

ABSTRACT

Although being among the closest gamma-ray bursts (GRBs), GRB 211211A poses challenges for its classification with partially inconclusive electromagnetic signatures. In this paper, we investigate four different astrophysical scenarios as possible progenitors for GRB 211211A: a binary neutron-star merger, a black-hole–neutron-star merger, a core-collapse supernova, and an r-process enriched core collapse of a rapidly rotating massive star (a collapsar). We perform a large set of Bayesian multi-wavelength analyses based on different models and priors to investigate which astrophysical scenarios and processes might have been related to GRB 211211A. Our analysis supports previous studies in which the presence of an additional component, likely related to r-process nucleosynthesis processes, is required to explain the observed light curves of GRB 211211A, as it can not solely be explained as a GRB afterglow. Fixing the distance to about 350 Mpc, i.e., the distance of the possible host galaxy SDSS J140910.47+275320.8, we find a statistical preference for the binary neutron-star merger scenario and estimate the component masses to be $1.55^{+0.54}_{-0.42}M_\odot$ and $1.34^{+0.25}_{-0.40}M_\odot$.

1. INTRODUCTION

The joint detection of gravitational waves (GWs) and electromagnetic (EM) signatures originating from the merger of binary neutron stars (BNSs) on August 17th 2017 (Abbott et al. 2017; Abbott et al. 2017) has been a breakthrough in multi-messenger astronomy. In addition to the GW signal GW170817, an associated kilonova, AT2017gfo, and a gamma-ray burst (GRB), GRB 170817A, were observed (Abbott et al. 2017). This multi-messenger detection allowed for an independent way of measuring the expansion rate of the Universe (Abbott et al. 2017), placed new constraints on the properties of supranuclear-dense matter (Bauswein et al. 2017; Ruiz et al. 2018; Radice et al. 2018; Most et al. 2018; Coughlin et al. 2019; Capano et al. 2020;

Dietrich et al. 2020; Huth et al. 2022), and proved that at least some short GRBs are connected to compact binary mergers (Abbott et al. 2017). However, it was also reported that short GRBs could originate from collapsars (Ahumada et al. 2021), indicating that the classification of astrophysical scenarios associated with GRBs is more complex (Zhang et al. (2021); Rossi et al. (2022)). Additional signatures associated with GRBs and their afterglows, such as kilonovae, significantly help to identify the origin of the progenitors. The kilonova AT2017gfo was certainly an exemplary case for such an EM signal, and spectral features connected to the creation of new elements (Watson et al. 2019; Domoto et al. 2022) in the outflowing material have possibly been observed. In addition to AT2017gfo,

there is a large number of kilonova candidates that could be connected to other GRB observations, e.g., GRB 050709, GRB 050724A, GRB 060614, GRB 061201, GRB 080905A, GRB 070724A, GRB 130603B, GRB 140903A, GRB 150101B, GRB 150424A, GRB 160821B, e.g., Tanvir et al. (2013); Berger et al. (2013); Yang et al. (2015); Zhang et al. (2007); Jin et al. (2015); Yang et al. (2015); Fox et al. (2005); Hjorth et al. (2005); Covino et al. (2006); Stratta et al. (2007); Berger et al. (2005); Malesani et al. (2007); Fong et al. (2016); Troja et al. (2018); Nicuesa Guelbenzu et al. (2012); Rowlinson et al. (2010); Berger et al. (2009); Kocevski et al. (2010); Kasliwal et al. (2017); Jin et al. (2018); Tanvir et al. (2015); Jin et al. (2018); cf. e.g. Ascenzi et al. (2019) for a review about some of these kilonova candidates. The most recent example that has to be added to the list is the kilonova candidate connected to GRB 211211A and its optical and near-infrared counterpart, e.g., Rastinejad et al. (2022), and Troja et al. (2022), and Mei et al. (2022).

GRB 211211A was discovered on the 11th December 2021 at 13:09:59 (UTC) by the Burst Alert Telescope (BAT) of the Swift Observatory (trigger 1088940, $SNR_{img} = 11.5$, D'Ai et al. 2021). The Fermi Gammaray Burst Monitor detected GRB 211211A independently at the exact same trigger time (trigger 211211549, $SNR_{ct} = 22.2$, Fermi GBM Team 2021). Moreover, the high-energy space instrument onboard Insight-HXMT detected GRB 211211A (trigger HEB211211548) during its routine search (Zhang et al. 2021). The GRB is characterized by a complex emission phase lasting approximately 10 s, and a longer, weaker extended emission for about 130 s in [15-350] keV (Stamatikos et al. 2021). Given this duration, GRB 211211A would be classified as a long GRB typically arising from the core-collapse of massive stars (e.g., Stanek et al. 2003; Levan et al. 2016) and not from compact binary mergers. Hence, for a scenario such as GRB 211211A, one would not necessarily expect to observe an associated kilonova.

About 70 s after the emergence of the prompt emission, Swift's X-ray Telescope (XRT) started observing the source. The X-ray observations showed bright emission (a flux of $3 \times 10^{-8} \mathrm{ergs}^{-1}\mathrm{cm}^{-2}$ in [0.3–10] keV) with an exponential decay lasting for hours after the trigger (Osborne et al. 2021). The Ultraviolet/Optical Telescope started its observations 92 s later and detected an optical counterpart within the X-ray localization error box. Given its close proximity to the galaxy SDSS J140910.47+275320, an intensive follow-up campaign including MITSuME, NEXT, the Nordic Optical Telescope, and the Calar Alto Observatory (Ito et al. 2021; Jiang et al. 2021; Malesani et al. 2021; de Ugarte Postigo

et al. 2021) was scheduled and the source was observed across multiple wavelengths. Based on these follow-up observations and the following analysis, it seems plausible that SDSS J140910.47+275320.8 was the host galaxy of GRB 211211A, at 98.6% confidence (Rastinejad et al. 2022). Details about the observation campaign are summarized in Rastinejad et al. (2022).

Rastinejad et al. (2022), Troja et al. (2022), and other groups explained these observations by invoking a kilonova in association with GRB 211211A. This was suggested for different reasons: (i) the profile of the prompt emission showed an initially complex structure followed by an extended softer emission, (ii) a predominant signature of a supernova was lacking for up to 17 days post-discovery, (iii) the color evolution of the optical counterpart had similar properties as AT2017gfo, and (iv) the offset of the GRB location concerning the center of the host galaxy was larger than for typical long GRBs.

Numerous other groups addressed the origin of GRB 211211A, e.g., Yang et al. (2022) suggested that it has similar properties as GRB 060614, another event associated with a kilonova candidate. They conclude that the significant excess in the near-infrared and optical afterglow at late observations points more towards a neutron star-white dwarf merger which leaves behind a rapidly spinning magnetar as a central engine providing additional heating to the ejecta. Waxman et al. (2022) showed that also thermal emission from dust could explain the observed near-infrared (NIR) data. Suvorov et al. (2022) mentioned a possible gamma-ray precursor before the main emission which was caused by the resonant shattering of one star's crust prior to the merger. In contrast, Gao et al. (2022) concluded the presence of a strong magnetic field from the precursor surrounding the central engine of the GRB. This would result in the prolongation of the accretion process and, thus, could explain the duration of the hard spiky emission detected for GRB 211211A. Similarly, Xiao et al. (2022) supposes that a magnetar participated in the merger and caused a quasi-periodic precursor. Gompertz et al. (2022) analyzed the spectra of the prompt emission of GRB 211211A by using synchrotron spectrum models and concluded that the spectral evolution can be explained by a transition from a fast-cooling to a slow cooling regime, favoring a BNS merger rather than a neutron-star–black-hole (NSBH) scenario. Finally, Barnes & Metzger (2023) investigated the possibility that collapsars could explain the origin of GRB 211211A and found that the afterglow-subtracted emission of GRB 211211A is in best agreement for collapsar models with high kinetic energies.

Following the discussion in the literature, we will use our nuclear physics and multi-messenger astrophysics (NMMA) framework (Pang et al. 2022)[1] to explore different astrophysical scenarios for the origin of GRB 211211A. We will consider the possibility of two merger scenarios, a BNS merger and an NSBH merger, and in addition two supernova scenarios, a core-collapse supernova, and an r-process enriched collapsar. For our model selection study, the NMMA framework allows us to simultaneously fit the observed data across the full electromagnetic range with multiple models, e.g., we can simultaneously employ GRB afterglow and kilonova models without the need of splitting the observational data in chunks and processing them separately, as done in – to our knowledge – previous studies of GRB 211211A.

2. OBSERVATIONAL DATA

In order to perform our model selection, we collect a set of multi-wavelength data observed for GRB 211211A (see Table 2). Concerning the GRB afterglow, we do not use any data from the prompt emission phase of the GRB in our analysis. This means that we use available X-ray data from the *Swift* X-ray Telescope, in particular, we use the 0.3 - 10 keV flux light curve observed at late times ($t = 10^4$ s after BAT trigger time) and convert it to 1 keV flux densities following Gehrels et al. (2008).

For our optical study, we followed Rastinejad et al. (2022) and included the refined analysis of Swift-UVOT observations. We contacted the authors of the observational teams responsible for the GCN reports, especially for those data which was not analyzed by Rastinejad et al. (2022). They provided us with offline results that we used in this article. For these data, we corrected the measurements by taking into account the foreground Galactic extinction $A_V = 0.048$ mag (Schlafly & Finkbeiner 2011). We excluded all photometric results from observations performed with the Johnson-Cousins UBVRI system as we do not compute simulated light curves in these passbands in our Bayesian approach. Moreover, we also excluded all photometric results from images taken without filters.

Finally, we use the 6 GHz radio detection of GRB 211211A observed 6.27 days after the initial trigger with a 5σ upper limit flux density of 16 μJy (Rastinejad et al. 2022). With regard to available GeV data, as reported in Zhang et al. (2022) and Mei et al. (2022), we do not include this data since our employed GRB model does not provide mechanisms to explain its origin.

We also re-analyzed data from the 2.3m telescope at the Centro Astronómico Hispano en Andalucía (CAHA),

equipped with the Calar Alto Faint Object Spectrograph (CAFOS) and find consistent results with respect to Rastinejad et al. (2022). Moreover, we exclude the detection measurement in the i band at 2.68 days post-discovery from our analysis since we find an upper limit of 22.6 mag at 5-σ with methods described in Aivazyan et al. (2022).

3. METHODS

3.1. *Bayesian Inference*

Our analysis is based on the nuclear physics and multi-messenger astronomy framework NMMA (Pang et al. 2022) that allows us to perform joint Bayesian inference runs of multi-messenger events containing GWs, kilonovae, supernovae, and GRB afterglow signatures. For this article, we extended the code infrastructure to include the description of r-process enriched collapsars following the model of Barnes & Metzger (2022).

We use the EM data of GRB 211211A to investigate which model or which combination of models describe the observational data best. According to Bayes' theorem, we compute posterior probability distributions, $p(\vec{\theta}|d, \mathbf{M})$, for model source parameters $\vec{\theta}$ under the hypothesis or model $\mathbf{M}$ with data d as

$$p(\vec{\theta}|d, \mathbf{M}) = \frac{p(d|\vec{\theta}, \mathbf{M})p(\vec{\theta}|\mathbf{M})}{p(d|\mathbf{M})} \rightarrow \mathcal{P}(\vec{\theta}) = \frac{\mathcal{L}(\vec{\theta})\pi(\vec{\theta})}{\mathcal{Z}(d)} ,$$
(1)

where $\mathcal{P}(\vec{\theta})$, $\mathcal{L}(\vec{\theta})$, $\pi(\vec{\theta})$, and $\mathcal{Z}(d)$ are the posterior, likelihood, prior, and evidence, respectively. In order to investigate the plausibility of competing models, we evaluate the odds ratio $\mathcal{O}_2^1$ for two models $\mathbf{M}_1$ and $\mathbf{M}_2$ which is given by

$$\mathcal{O}_2^1 = \frac{p(d|\mathbf{M}_1)}{p(d|\mathbf{M}_2)} \frac{p(\mathbf{M}_1)}{p(\mathbf{M}_2)} \equiv \mathcal{B}_2^1 \Pi_2^1,$$
(2)

where $\mathcal{B}_2^1$ and Π_2^1 are the Bayes factor and the prior odds, respectively. Under the assumption that the different astrophysical scenarios considered here are equally likely to explain GRB 211211A, we impose unity prior odds, i.e., $\Pi_2^1 = 1$, for all comparisons of models describing these scenarios. Therefore, we simply compute the Bayes factor $\mathcal{B}_2^1$. In our study, we report the natural logarithm of the Bayes factor,

$$\ln \mathcal{B}_{\mathrm{ref}}^1 = \ln \left(\frac{p(d|\mathbf{M}_1)}{p(d|\mathbf{M}_{\mathrm{ref}})} \right) ,$$
(3)

relative to our best fitting model as a reference (ref.), which we will denote as $\ln \mathcal{B}_{\mathrm{ref}}$ hereafter. Following Jeffreys (1961) and Kass & Raftery (1995), we interpret $\ln \mathcal{B}_{\mathrm{ref}}^1$ as the evidence favoring our reference model as:

---

[1] https://github.com/nuclear-multimessenger-astronomy

$$\ln[\mathcal{B}_{\mathrm{ref}}^1] < -4.61 \qquad \text{decisive evidence,}$$
$$-4.61 \leq \ln[\mathcal{B}_{\mathrm{ref}}^1] \leq -2.30 \qquad \text{strong evidence,}$$
$$-2.30 \leq \ln[\mathcal{B}_{\mathrm{ref}}^1] \leq -1.10 \qquad \text{substantial evidence,}$$
$$-1.10 \leq \ln[\mathcal{B}_{\mathrm{ref}}^1] \leq 0 \qquad \text{no strong evidence.}$$

However, we point out that these classifications should only be considered as estimates and that the Bayes factor is generally a continuous quantity. In addition to the Bayes factor, we also provide information about the ratio of the maximum likelihood, or the difference of the maximum log-likelihood point estimates $\ln[\mathcal{L}_2^1(\hat{\theta})]$ supporting our analysis in Sec. 4.1. We will denote this as $\ln[\mathcal{L}_{\mathrm{ref}}(\hat{\theta})]$ when we compare the maximum log-likelihood against our reference model.

3.2. Employed models

As described in the introduction, we investigate four different scenarios in our study from which GRB 211211A could have emerged. In particular, we consider two merger scenarios: a BNS merger and an NSBH merger, and two supernova cases: a phenomenological long GRB supernova template and an r-process enriched collapsar scenario.

BNS scenario: For this case, we use the kilonova models of Dietrich et al. (2020) (hereafter 'BNS-KN-Bulla') and of Kasen et al. (2017) (hereafter 'BNS-KN-Kasen'). BNS-KN-Bulla is based on the time-dependent three-dimensional Monte Carlo radiation transfer code possis (Bulla (2019), Bulla, Mattia (2022)), which computes light curves, spectra, and luminosities for kilonovae depending on the viewing-angle θ_{Obs}. The ejected material is classified through the dynamical ejecta mass, $M_{\mathrm{ej}}^{\mathrm{dyn}}$, and the disk-wind ejecta mass, $M_{\mathrm{ej}}^{\mathrm{wind}}$. The tidal dynamical ejecta component is assumed to be distributed within a half opening angle Φ. In the same way, BNS-KN-Kasen uses the multi-dimensional Monte Carlo code sedona that solves the multi-wavelength radiation transport equation in a relativistically expanding medium (Kasen et al. (2006); Roth & Kasen (2015)). In this paper, we use the one-dimensional model provided by Kasen et al. (2017), which assumes spherical symmetry and uniform composition for our analysis. The model, 'BNS-KN-Kasen', depends on the ejecta mass, M_{ej}, a characteristic expansion velocity, v_{ej}, and the mass fraction of lanthanides, X_{lan}, which affects the opacity.

NSBH scenario: For this case, we also use a possis model grid of KN spectra tailored to NSBH mergers which was used in the study of Anand et al. (2021) (hereafter 'NSBH-KN-Bulla'). This model depends on the same model parameters as BNS-KN-Bulla but excludes the dependence on the half opening angle of the dynamical ejecta, fixed to $\Phi = 30°$.

Supernova: In order to assess the possibility of a typical core-collapse supernova (CCSN) associated with a long GRB, we use the nugent-hyper model from sncosmo (Levan et al. 2005) with the absolute magnitude, S_{max}, as the main free parameter. This model is a template constructed from observations of the supernova SN1998bw associated with the long GRB 980425 and is hereafter abbreviated as 'SN98bw'.

r-process enriched Collapsar: Rapidly rotating massive star core collapses (Burbidge et al. 1957; Qian & Woosley 1996) are another possible astrophysical site for r-process nucleosynthesis. As massive stars undergo a core collapse, material is disrupted and forms an accretion disk which can become neutron-rich through weak interactions (Beloborodov 2003) and can launch winds which power emission of r-process-enriched core-collapse SNe (rCCSNe). We use the semi-analytic model for rCCSNe of Barnes & Metzger (2022) (hereafter denoted as 'SNCol'). The model depends on five free parameters: the total ejecta mass, M_{ej}, a characteristic ejecta velocity, v_{ej}, the ^{56}Ni mass, M_{Ni}, the r-process material mass, M_{rp}, and the mixing coordinate, Ψ_{mix}. The ejecta are assumed to be spherically symmetric, with r-process elements of mass m_{rp} concentrated in an inner core whose total mass is $\Psi_{\mathrm{mix}} m_{\mathrm{ej}}$, with $\Psi_{\mathrm{mix}} \leq 1$. An r-process-free envelope surrounds the core, and 56-Ni is distributed uniformly throughout the core and the envelope. The velocity v_{ej} is defined such that the total kinetic energy of the ejecta E_{kin} is equal to $\frac{1}{2} M_{\mathrm{ej}} v_{\mathrm{ej}}^2$.[2]

GRB afterglow: For modeling the GRB afterglow light curves, we employ the semi-analytic model of van Eerten et al. (2010) and Ryan et al. (2020), available in the public afterglowpy library (denoted as 'GRB-M'). The model computes GRB afterglow emission and takes the following free parameters as input: the isotropic kinetic energy, $E_{\mathrm{K,iso}}$, the viewing angle, θ_{Obs}, the half-opening angle of the jet core, θ_c, the outer truncation angle of the jet, θ_w, the interstellar medium density, n, the electron energy distribution index, p, and the fractions of the shock energy that go into electrons, ϵ_e, and magnetic fields, ϵ_B. The model allows for several angular structures of the GRB jet. For our simulations, we assume a Gaussian or a top-hat jet structure (hereafter, 'Gauss' and 'top')[3]. It is important to note that, while we try to be agnostic concerning GRB 211211A's

---

[2] Barnes & Metzger (2023) also compared rCCSNe with observational data from GRB 211211A. However, not within a Bayesian approach as employed here and with an updated version of their model originally described in Barnes & Metzger (2022).

[3] In addition, we tested a power law jet structure for which we found consistent results.

origin, the GRB-M model that we employ has some limitations. Specifically, it does not include the emission from the reverse shock that might be important at early times. Additionally, it does not include the wind-like interstellar medium, which is expected in the case of a collapsar.

In Fig. 1, we summarize our approach to analyze GRB 211211A based on the data set described in Sec. 2. We employ two different priors for the luminosity distance, i.e., a narrow Gaussian luminosity distance prior centered around 350 Mpc as reported by Rastinejad et al. (2022) and a uniform prior on the luminosity distance ranging between 0 and 1000 Mpc. This allows us to investigate the potential influence of the distance on the GRB classification. Furthermore, we employ five models or model combinations to describe the different astrophysical scenarios. For the choice of a Gaussian luminosity distance prior, we report the prior settings for all parameters of the employed models in Table 3. Moreover, we use two different GRB jet types, totaling in 20 Bayesian inference simulations.

4. MULTI-WAVELENGTH ANALYSES

In the following three subsections, 4.1-4.3, we discuss our results for a narrow Gaussian prior on the luminosity distance in order to compare with previous studies. In subsection 4.4, we will investigate the influence of the distance prior choice and employ a wide uniform prior on the luminosity distance.

4.1. *Model Comparison*

As indicated in the introduction, one of the main differences between previous studies and our work is that most previous works fitted first the X-ray and radio data with a GRB afterglow model, and then used the afterglow-subtracted optical and near-infrared photometry for fitting a kilonova model. In contrast, we perform a joint analysis of the GRB afterglow and a possible additional contribution such as a kilonova signature or emission from a rCCSN or CCSN. Moreover, in order to consider systematic uncertainties arising from different assumptions made in each model, we employ a 1 mag uncertainty in our simulations.

In Table 1, we summarize our main findings for the investigated astrophysical scenarios. We found that the BNS-GRB$_{\mathrm{top}}^{\mathrm{Kasen}}$ model describes the observational data best, and hence, we pick it as our reference model. Consequently, the Bayes factors and likelihood ratios in Table 1 are reported relative to this best-fit inference run. With reference to Table 1, we show the maximum log-likelihood light curve fits in Fig. 2 for each assessed scenario, which we will refer to as "best-fitting light curves" hereafter.

Comparing only the two different BNS kilonova models, we find that differences in the Bayes factors are of order unity. We interpret this as a measure of the systematic model uncertainty for different employed kilonova models, given that both BNS-GRB$_{\mathrm{Gauss/top}}^{\mathrm{Bulla}}$ and BNS-GRB$_{\mathrm{Gauss/top}}^{\mathrm{Kasen}}$ should describe the same physical system. It is worth pointing out that statistical uncertainties, as stated in the table, are noticeably smaller than model differences, i.e., our results are dominated by systematic uncertainties in the underlying light curve models.

Considering the differences between the NSBH and BNS scenarios, we find strong evidence that GRB 211211A was connected to a BNS rather than an NSBH system. This is reflected both in Bayes factors as well as maximum log-likelihood values as shown in Table 1. Comparing the respective best fitting light curves in Fig. 2, we see that NSBH-GRB$_{\mathrm{top}}^{\mathrm{Bulla}}$ fits the NIR-band data worse compared to GRB$_{\mathrm{top}}^{\mathrm{Kasen}}$.

With regard to the relative Bayes factors for the collapsar scenario, we find that there is decisive evidence that a BNS scenario is preferred over a collapsar origin for GRB 211211A. However, it is important to note that the collapsar model depends on more parameters. Because of this, Occam's razor penalizes the model despite its ability to describe the observational data; cf. Fig. 2. This ability to describe and fit the observational data can be estimated from the maximum likelihood ratio results as given in Tab. 1.

As indicated by Rastinejad et al. (2022), and confirmed by our study, we find that a Ni-powered SN event or an SN-GRB scenario is noticeably less favored compared to a BNS merger. This is depicted in Fig. 2 in which SN98bw-GRB$_{\mathrm{top}}^{\mathrm{Bulla}}$ fails to fit late-time NIR data, resulting in a larger, negative log-likelihood ratio.

Finally, our study confirms that the BNS-GRB$_{\mathrm{top}}^{\mathrm{Kasen}}$ scenario provides decisive evidence when compared with GRB$_{\mathrm{top}}$-M simulations, even though the latter sampled over fewer parameters in respective parameter estimation runs. Considering the impact of the choice of a Gaussian vs. top-hat jet structure on our Bayes factor results, we find a slight preference for the top-hat jet structure for all assessed scenarios, except for NSBH-GRB$_{\mathrm{Gauss}}^{\mathrm{Bulla}}$.

4.2. *Presence of an additional component*

Given the overall narrative that GRB 211211A was a GRB connected to a kilonova, we study the ability of the GRB-M with top-hat jet structure to describe the observational data and compare this with two BNS merger scenarios. For this purpose, we show the best-fitting light curves for BNS-GRB$_{\mathrm{top}}^{\mathrm{Bulla}}$, BNS-GRB$_{\mathrm{top}}^{\mathrm{Kasen}}$, and GRB$_{\mathrm{top}}$ in Fig. 3.
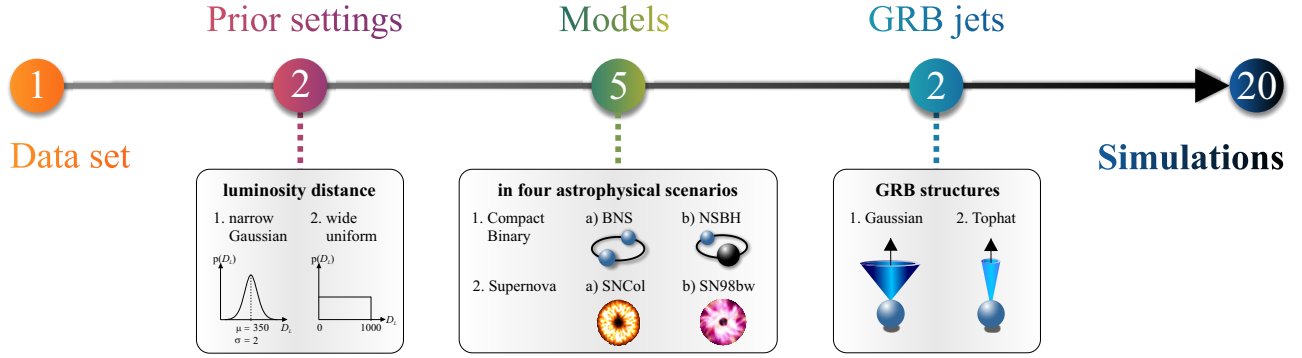
Figure 1. Schematic illustration of our comprehensive Bayesian inference campaign performed to analyze GRB 211211A. We use one observational data set as described in Sec. 2, two prior settings in which we mainly vary the luminosity distance prior while prior settings for other model parameters remained fixed and are reported in Table 3, five models (including two different BNS kilonova models) or model combinations for four different astrophysical scenarios, and two GRB jet types (Gaussian and top-hat), totaling in 20 Bayesian inferences.

Name	Astrophysical Processes	GRB Jet Structure	Model dimension	Bayes factor $\ln[\mathcal{B}^1_{\mathrm{ref}}]$	Likelihood $\ln[\mathcal{L}^1_{\mathrm{ref}}(\hat{\theta})]$
BNS-GRB$^{\mathrm{Kasen}}_{\mathrm{top}}$	Kilonova + GRB	Tophat	11	ref.	ref.
BNS-GRB$^{\mathrm{Kasen}}_{\mathrm{Gauss}}$	Kilonova + GRB	Gaussian	12	-1.01 ± 0.10	-0.33
BNS-GRB$^{\mathrm{Bulla}}_{\mathrm{top}}$	Kilonova + GRB	Tophat	11	-0.49 ± 0.10	-1.15
BNS-GRB$^{\mathrm{Bulla}}_{\mathrm{Gauss}}$	Kilonova + GRB	Gaussian	12	-1.59 ± 0.10	-2.13
NSBH-GRB$_{\mathrm{top}}$	Kilonova + GRB	Tophat	11	-3.76 ± 0.10	-3.82
NSBH-GRB$_{\mathrm{Gauss}}$	Kilonova + GRB	Gaussian	12	-2.08 ± 0.10	-4.16
SNCol-GRB$_{\mathrm{top}}$	rCCSNe + GRB	Tophat	14	-10.42 ± 0.11	-3.04
SNCol-GRB$_{\mathrm{Gauss}}$	rCCSNe + GRB	Gaussian	15	-10.74 ± 0.11	-3.58
SN98bw-GRB$_{\mathrm{top}}$	CCSNe + GRB	Tophat	8	-6.93 ± 0.10	-8.14
SN98bw-GRB$_{\mathrm{Gauss}}$	CCSNe + GRB	Gaussian	9	-8.05 ± 0.10	-8.13
GRB$_{\mathrm{top}}$	GRB	Tophat	8	-6.04 ± 0.10	-7.10
GRB$_{\mathrm{Gauss}}$	GRB	Gaussian	9	-6.96 ± 0.10	-7.33

Table 1. Results for the logarithmic Bayes factors, $\ln[\mathcal{B}^1_{\mathrm{ref}}]$, and maximum logarithmic likelihood ratios, $\ln[\mathcal{L}^1_{\mathrm{ref}}(\hat{\theta})]$, relative to the best-fit, joint inference using BNS-GRB$^{\mathrm{Kasen}}_{\mathrm{top}}$ (ref.). The four investigated scenarios of possible astrophysical origins (BNS, NSBH, SNCol, and SN98bw) are each being assessed assuming a Gaussian or a Top-hat jet structure. As reference, we list results for a stand-alone GRB model investigation for both jet structures.

We find that the GRB-M model achieves a good representation of the data in almost all bands, except for the i-band and K-band data at late times (shown in Fig. 3). In contrast, the joint model inferences of BNS-GRB$^{\mathrm{Bulla}}_{\mathrm{top}}$ and BNS-GRB$^{\mathrm{Kasen}}_{\mathrm{top}}$ achieve a better representation of i-band and K-band data and the observational data points lie within the estimated 1 magnitude uncertainty (shaded band) of the best-fit light curves. Hence, our analysis suggests that an additional source of energy generation is required to generate bright light curves at late times in the i- and K-band and to fit the observed data.

We have further investigated the impact of late-time i-band data on our inference results, in particular, we have performed analysis runs, not shown in Fig. 3, in which

we have excluded i-band data observed with Gemini-GMOS two days after trigger time (see Table 2) for BNS-GRB$^{\mathrm{Bulla}}_{\mathrm{top}}$, BNS-GRB$^{\mathrm{Kasen}}_{\mathrm{top}}$, and GRB$_{\mathrm{top}}$. We found that BNS-GRB$^{\mathrm{Bulla}}_{\mathrm{top}}$, BNS-GRB$^{\mathrm{Kasen}}_{\mathrm{top}}$, and GRB$_{\mathrm{top}}$ perform almost identically, and predict similar light curves in the i-band, but also in all other bands. This shows that late i-band data points are the main source of difference between the standalone GRB model and BNS-GRB models.

### 4.3. *Source properties of the potential compact binary mergers*

For the scenario that GRB 211112A was connected to a compact binary merger, which is favored by our analysis, we now determine the source properties of the potential progenitor system. For this purpose, we use the
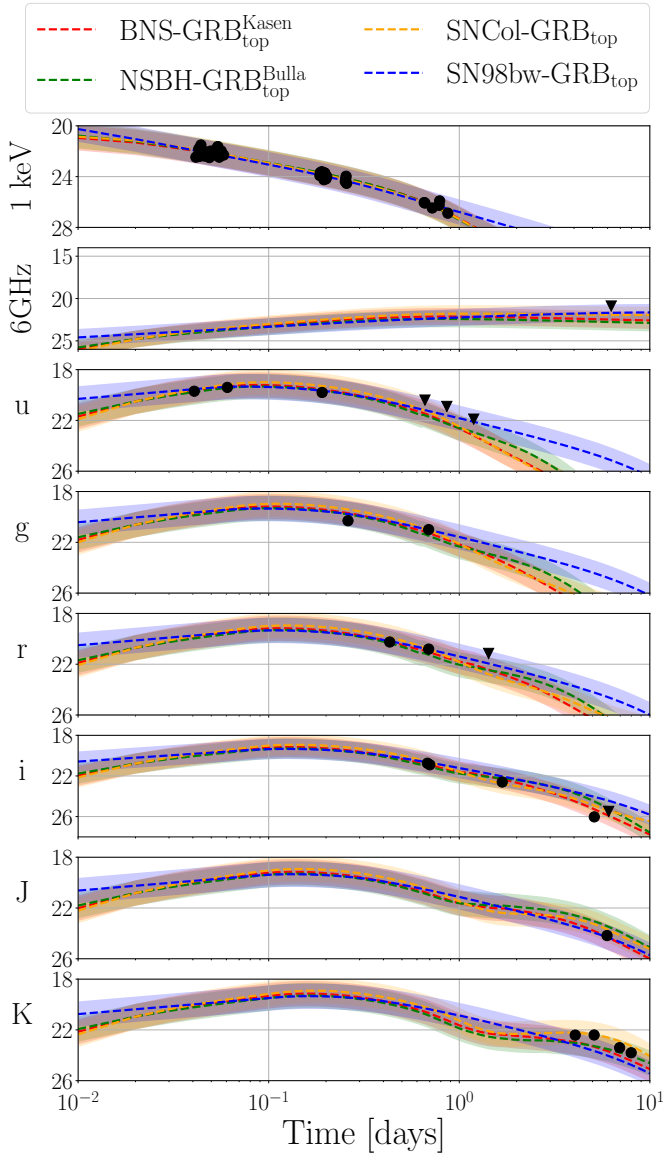
Figure 2. Best fitting light curve from joint Bayesian inferences listed in Table 1 for possible scenarios: BNS-GRB$_{\rm top}^{\rm Kasen}$ (red), NSBH-GRB$_{\rm top}$ (green), SNCol-GRB$_{\rm top}$ (orange), and SN98bw-GRB$_{\rm top}$ (blue). The observational data of GRB 211211A in X-ray-1keV, radio-6GHz, UV, optical, and NIR band as discussed in Sec. 2 are shown as black dots, whereas black triangles refer to upper detection limits.

inferred GRB afterglow and kilonova properties for both BNS-KN-Kasen and BNS-KN-Bulla and connect information about the ejecta and debris disk to the BNS properties following Dietrich et al. (2020); cf. Henkel et al. (2022) for a recent discussion about uncertainties in the employed numerical-relativity informed phenomenological relations.

In Fig. 4, we show our inference results for a possible BNS source using BNS-GRB$_{\rm top}^{\rm Kasen}$, BNS-GRB$_{\rm Gauss}^{\rm Kasen}$, and BNS-GRB$_{\rm top}^{\rm Bulla}$ and contrast these to the prior probabil-
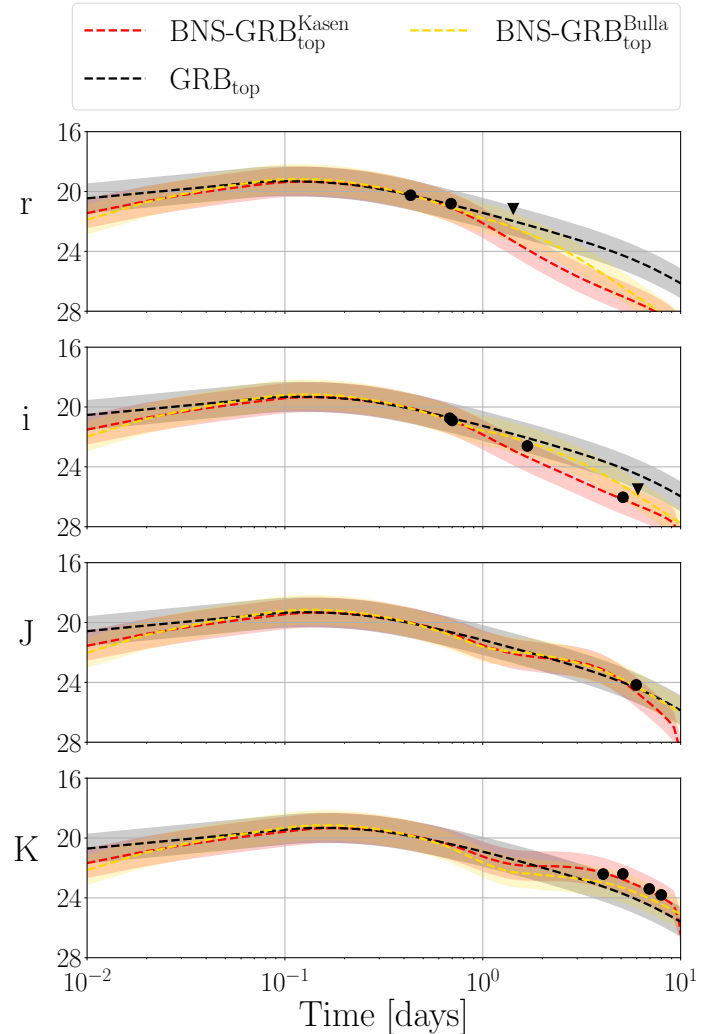
Figure 3. Best-fitting light curves from joint Bayesian inferences of BNS-GRB$_{\rm top}^{\rm Bulla}$ (yellow) and BNS-GRB$_{\rm top}^{\rm Kasen}$ (red) compared to a stand-alone GRB$_{\rm top}$ inference (black) for optical and NIR bands on a logarithmic time scale in days since trigger time.

ity regions for each parameter, in order to show how constraining the observational data is. Comparing inference results for BNS-GRB$_{\rm Top}^{\rm Kasen}$ and BNS-GRB$_{\rm Gauss}^{\rm Kasen}$, we find that estimated source masses and tidal deformabilies are very similar. For the top-hat jet structure simulation, we find that a BNS merger with a primary mass of $1.55_{-0.42}^{+0.54} M_\odot$ and a secondary mass of $1.34_{-0.40}^{+0.25} M_\odot$ was the likely progenitor. The associated dimensionless tidal deformability of the system lies within $\tilde{\Lambda} = 299_{-274}^{+1041}$. With regard to a similar analysis for BNS-GRB$_{\rm Top}^{\rm Bulla}$, we find a primary mass of $1.56_{-0.34}^{+0.43} M_\odot$ and a secondary mass of $1.29_{-0.29}^{+0.20} M_\odot$. The corresponding tidal deformability is 353_{-264}^{+598}. Comparing estimated masses for BNS-GRB$_{\rm Top}^{\rm Kasen}$ and BNS-GRB$_{\rm Top}^{\rm Bulla}$, we find overall good agreement within the stated uncertainties. Con-

cerning the tidal deformability, we find that the BNS-KN-Bulla model provides tighter constraints compared to those extracted with the BNS-KN-Kasen model. We expect this deviation to originate from the fact that the BNS-KN-Bulla model provides more detailed information on the estimated wind and dynamical ejecta masses, while the BNS-KN-Kasen model provides a generic estimate of the total ejecta mass.

Overall, our estimated masses are consistent with Rastinejad et al. (2022), who concluded that GRB 211211A originated from a 1.4 $M_\odot$+1.3 $M_\odot$ BNS merger. We expect that the remaining small differences are caused by the different analysis of the observed GRB 211211A data and by the fact that Rastinejad et al. (2022) assumed the inclination angle, under which the binary was observed, to be zero. Moreover, Rastinejad et al. (2022) assumed a fixed equation of state from the EOS set of Dietrich et al. (2020) using additional information from Nicholl et al. (2021). In contrast, we leave the inclination angle as a free parameter in our analysis and use the updated EOS set of Huth et al. (2022). This set incorporates information from theoretical nuclear-physics computations and from astrophysical observations of neutron stars such as Dietrich et al. (2020), but also heavy-ion collision experimental data. With regard to investigated binary merger scenarios, we find that the inferred inclination angle is around $\theta_{\rm Obs} \approx 0.02^{+0.05}_{-0.02}$, while larger inclination angles of approximately $\theta_{\rm Obs} \approx 0.07^{+0.11}_{-0.06}$ are estimated for the two considered supernova scenarios (see Table 3).

Rastinejad et al. (2022) deduced a total r-process ejecta mass of $M_{\rm ej} = 0.047^{+0.026}_{-0.011}M_\odot$, of which 0.02 $M_\odot$ correspond to lanthanide-rich ejecta, 0.01 $M_\odot$ to intermediate-opacity ejecta, and 0.01 $M_\odot$ to lanthanide-free material. With our reference inference result from BNS-GRB$^{\rm Kasen}_{\rm top}$, we find a total ejecta mass of $M^{\rm BNS}_{\rm ej, Kasen} = 0.021^{+0.017}_{-0.013}M_\odot$ which is broadly in agreement given the uncertainties. Concerning our analysis based on BNS-GRB$^{\rm Bulla}_{\rm top}$, we found a total ejecta mass of $M^{\rm BNS}_{\rm ej} = 0.031^{+0.033}_{-0.018}M_\odot$, of which $0.015M_\odot$ can be attributed to lanthanide-rich ejecta, $0.011M_\odot$ to intermediate-opacity mass, and $0.002M_\odot$ to lanthanide-free material.

For completeness, we have performed a similar investigation for our NSBH-GRB$_{\rm top}$ and NSBH-GRB$_{\rm Gauss}$ models to infer the corresponding NSBH properties by making use of the relations provided in Foucart et al. (2018) and Krüger & Foucart (2020). Although the observational data does not provide a strong constraint on the NSBH source properties, our NSBH-GRB$_{\rm top}$ analysis suggests that an NSBH merger with a BH mass
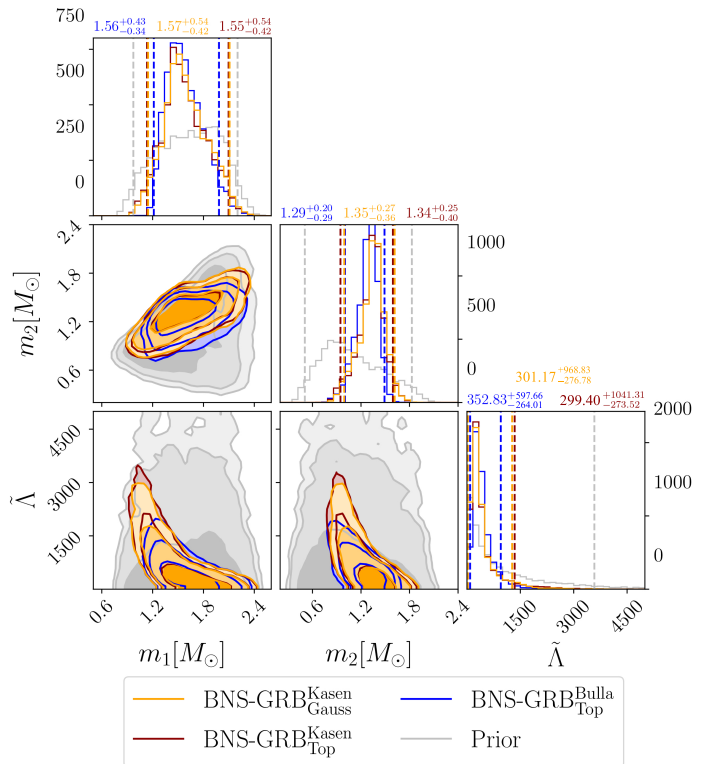
Figure 4. Component masses $m_{1,2}$ and the dimensionless tidal deformability $\tilde{\Lambda}$ based on our inference results of BNS-GRB$^{\rm Kasen}_{\rm Gauss}$ (orange), BNS-GRB$^{\rm Kasen}_{\rm Top}$ (red) and BNS-GRB$^{\rm Bulla}_{\rm Top}$ (blue). Different shadings mark the 68%, 95%, and 99% confidence intervals. For the 1D posterior probability distributions, we give the 90% confidence interval (dashed lines) and report median values above each panel. Grey shaded areas give the prior probability regions.

of $3.18^{+8.54}_{-2.34}M_\odot$ and an NS mass of $1.39^{+0.83}_{-0.85}M_\odot$ could have been the progenitor of GRB 211211A, with a total ejecta mass of $M^{\rm NSBH}_{\rm ej} = 0.008^{+0.012}_{-0.006} M_\odot$. Likewise, the BH spin is weakly constrained to $\chi_1 = 0.00^{+0.57}_{-0.74}$ for the NSBH-GRB$_{\rm top}$ inference. Our inferred NS masses are in agreement with previous GW population analyses (Abbott et al. 2019, 2021a,b) and with the maximum non-spinning NS mass of $2.7^{+0.5}_{-0.4}M_\odot$ estimated at 90% credibility by Ye & Fishbach (2022). Within the estimated uncertainties, the inferred BH mass is close to the NSBH mass gap for which the lightest BH masses were estimated to be $\sim 5M_\odot$ (Özel et al. 2010; Farr et al. 2011).

4.4. *Influence of the prior choice*

Finally, we discuss the influence of a different luminosity distance prior on our results. The distance of GRB 211211A was relatively precisely estimated based on the redshift of the potential host galaxy, $z = 0.0763 \pm 0.0002$ (Rastinejad et al. 2022). However, we are generally interested in the influence of a

wide uniform luminosity distance prior on our results. For this reason, we widen the prior range and allow a distance between 0 and 1000 Mpc.

Following the procedure in Sec. 4.1, we have computed the logarithmic Bayes factors and found that BNS-GRB$_{\rm top}^{\rm Kasen}$ remains to be the best-fitting model. Moreover, the differences in logarithmic Bayes factors between BNS-KN-Bulla and BNS-KN-Kasen remain the same. Overall, the differences with regard to the individual Bayes factors as presented in Tab. 1 are small. However, the SN and collapsar scenarios are now equally disfavored. Hence, our main conclusions remain valid also for the wider distance prior.

We have investigated the posterior probability distributions obtained for a wide uniform distance prior and compare these with the ones obtained for a narrow Gaussian distance prior setting. In Fig. 5, we show an example for the obtained luminosity distance and the total ejecta mass distributions using GRB$_{\rm top}^{\rm Kasen}$. As can be seen, the wide distance prior leads to a noticeably weaker constraint on the distance and the total ejecta mass. The latter is caused by a degeneracy between the luminosity distance and the ejecta mass. Generally, larger ejecta masses could compensate for larger distances and vice versa, which explains the shape of the 2D correlation plot of Fig. 5. Similarly (not shown in the figure), also the SNCol model predicts higher ejecta masses for larger distances. With respect to the SN-GRB and the GRB inferences, the GRB isotropic energy, $\log_{10}(E_{\rm K,iso})$, tends to increase for larger distances, which is expected as brighter signals can be detected to further distances.

5. CONCLUSION

In this paper, we have performed multiple multi-wavelength analyses for GRB 211211A assuming four different scenarios, i.e., a BNS merger, an NSBH merger, an rCCSN, as well as a CCSN. On the basis of joint multi-wavelength Bayesian inferences combining respective kilonova or SN models with a gamma-ray burst afterglow model, we studied for which scenario we find the highest statistical evidence to explain the data. We summarize our main conclusions:

(i) We find strong statistical evidence for a BNS merger scenario; cf. Table 1. However, we can not fully rule out other scenarios.

(ii) Our study confirms that GRB 211211A can not solely be explained as a GRB afterglow and that an additional emission process (likely related to r-process nucleosynthesis) is required for a good
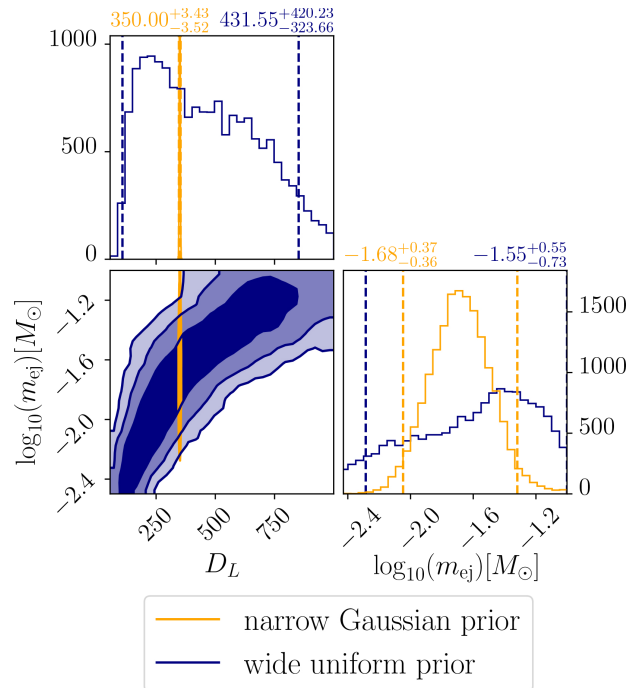
Figure 5. Corner plot for BNS-GRB$_{\rm top}^{\rm Kasen}$ with a narrow Gaussian luminosity distance prior centered around 350 Mpc (orange) and a wide uniform luminosity distance prior ranging up to 1000 Mpc (blue). The inferred model parameters are shown at 68%, 95%, and 99% confidence (shadings from light to dark). For the 1D posterior probability distributions, we report the median values and show the 90% confidence intervals as dashed lines.

description of the observational data, mostly in late i-band and K-band data.

(iii) Assuming a BNS origin, our study suggests that this system was a $1.55^{+0.54}_{-0.42}M_\odot$ - $1.34^{+0.25}_{-0.40}M_\odot$ binary, leading to a total ejecta mass of $M_{\rm ej}^{\rm BNS} = 0.021^{+0.017}_{-0.013}M_\odot$. Assuming a NSBH origin of GRB 211211A, our study suggests a $1.39^{+0.83}_{-0.85}$ - $3.18^{+8.54}_{-2.34}M_\odot$ system with a total ejecta mass of $M_{\rm ej}^{\rm NSBH} = 0.008^{+0.012}_{-0.006}\ M_\odot$.

(iv) The results discussed in Sec. 4.2 showed that near-infrared data at late times are essential to investigate the astrophysical origin of interesting transient objects.

6. ACKNOWLEDGEMENT

REFERENCES

Abbott, B. P., Abbott, R., Abbott, T. D., et al. 2017, ApJL, 848, L13

Abbott, B. P., Abbott, R., Abbott, T. D., et al. 2017, Phys. Rev. Lett., 119, 161101. https://link.aps.org/doi/10.1103/PhysRevLett.119.161101

Abbott, B. P., Abbott, R., Abbott, T. D., et al. 2017, ApJL, 848, L12

Abbott, B. P., et al. 2017, Nature, 551, 85

—. 2019, Phys. Rev. X, 9, 031040

Abbott, R., et al. 2021a, arXiv:2111.03606

—. 2021b, Phys. Rev. X, 11, 021053

Ahumada, T., Singer, L. P., Anand, S., et al. 2021, Nature Astronomy, 5, 917

Aivazyan, V., Almualla, M., Antier, S., et al. 2022, MNRAS, 515, 6007

Anand, S., et al. 2021, Nature Astron., 5, 46

Ascenzi, S., et al. 2019, Mon. Not. Roy. Astron. Soc., 486, 672

Barnes, J., & Metzger, B. D. 2022, The Astrophysical Journal Letters, 939, L29. https://dx.doi.org/10.3847/2041-8213/ac9b41

Barnes, J., & Metzger, B. D. 2023, arXiv e-prints, doi:10.48550/ARXIV.2301.01389

Bauswein, A., Just, O., Janka, H.-T., & Stergioulas, N. 2017, Astrophys. J. Lett., 850, L34

Beloborodov, A. M. 2003, Astrophys. J., 588, 931

Berger, E., Cenko, S. B., Fox, D. B., & Cucchiara, A. 2009, ApJ, 704, 877

Berger, E., Fong, W., & Chornock, R. 2013, Astrophys. J. Lett., 774, L23

Berger, E., Price, P. A., Cenko, S. B., et al. 2005, Nature, 438, 988 EP . http://dx.doi.org/10.1038/nature04238

Buchner, J., Georgakakis, A., Nandra, K., et al. 2014, Astron. Astrophys., 564, A125

Bulla, M. 2019, Mon. Not. Roy. Astron. Soc., 489, 5037

Bulla, Mattia. 2022, arXiv:2211.14348

Burbidge, E. M., Burbidge, G. R., Fowler, W. A., & Hoyle, F. 1957, Rev. Mod. Phys., 29, 547. https://link.aps.org/doi/10.1103/RevModPhys.29.547

Capano, C. D., Tews, I., Brown, S. M., et al. 2020, Nature Astron., 4, 625

Coughlin, M. W., Dietrich, T., Margalit, B., & Metzger, B. D. 2019, Mon. Not. Roy. Astron. Soc., 489, L91

Coughlin, M. W., Dietrich, T., Doctor, Z., et al. 2018, Monthly Notices of the Royal Astronomical Society, 480, 3871

Covino, S., Malesani, D., Israel, G. L., et al. 2006, A&A, 447, L5

D'Ai, A., Ambrosi, E., D'Elia, V., et al. 2021, GRB Coordinates Network, 31202, 1

D'Avanzo, P., Rossi, A., Malesani, D. B., et al. 2021, GRB Coordinates Network, 31242, 1

de Ugarte Postigo, A., Kann, D. A., Thoene, C., et al. 2021, GRB Coordinates Network, 31218, 1

Dietrich, T., Coughlin, M. W., Pang, P. T. H., et al. 2020, Science, 370, 1450

Domoto, N., Tanaka, M., Kato, D., et al. 2022, Astrophys. J., 939, 8

Farr, W. M., Sravan, N., Cantrell, A., et al. 2011, The Astrophysical Journal, 741, 103

Fermi GBM Team. 2021, GRB Coordinates Network, 31211, 1

Fong, W., Margutti, R., Chornock, R., et al. 2016, The Astrophysical Journal, 833, 151. http://stacks.iop.org/0004-637X/833/i=2/a=151

Foucart, F., Hinderer, T., & Nissanke, S. 2018, Physical Review D, 98, doi:10.1103/physrevd.98.081501

Fox, D. B., Frail, D. A., Price, P. A., et al. 2005, Nature, 437, 845 EP . http://dx.doi.org/10.1038/nature04189

Gao, H., Lei, W.-H., & Zhu, Z.-P. 2022, arXiv e-prints, arXiv:2205.05031

Gehrels, N., Barthelmy, S. D., Burrows, D. N., et al. 2008, ApJ, 689, 1161

Gompertz, B. P., Ravasio, M. E., Nicholl, M., et al. 2022, arXiv e-prints, arXiv:2205.05008

Henkel, A., Foucart, F., Raaijmakers, G., & Nissanke, S. 2022, arXiv:2207.07658

Hjorth, J., Watson, D., Fynbo, J. P. U., et al. 2005, Nature, 437, 859

Huth, S., et al. 2022, Nature, 606, 276

Ito, N., Hosokawa, R., Murata, K. L., et al. 2021, GRB Coordinates Network, 31217, 1

Jeffreys, H. 1961, Theory of Probability (Oxford University Press)

Jiang, S. Q., Zhu, Z. P., Fu, S. Y., et al. 2021, GRB Coordinates Network, 31213, 1

Jin, Z.-P., Li, X., Cano, Z., et al. 2015, ApJL, 811, L22

Jin, Z.-P., Li, X., Wang, H., et al. 2018, ApJ, 857, 128

Kasen, D., Metzger, B., Barnes, J., Quataert, E., & Ramirez-Ruiz, E. 2017, Nature, 551, 80

Kasen, D., Thomas, R. C., & Nugent, P. 2006, Astrophys. J., 651, 366

Kasliwal, M. M., Korobkin, O., Lau, R. M., Wollaeger, R., & Fryer, C. L. 2017, ApJL, 843, L34

Kass, R. E., & Raftery, A. E. 1995, Journal of the American Statistical Association, 90, 773

Kocevski, D., Thöne, C. C., Ramirez-Ruiz, E., et al. 2010, MNRAS, 404, 963

Krüger, C. J., & Foucart, F. 2020, Phys. Rev. D, 101, 103002

Kumar, H., Bhalerao, V., Gupta, R., et al. 2021, GRB Coordinates Network, 31227, 1

Levan, A., Crowther, P., de Grijs, R., et al. 2016, SSRv, 202, 33

Levan, A., et al. 2005, Astrophys. J., 624, 880

Malesani, D., Covino, S., D'Avanzo, P., et al. 2007, A&A, 473, 77

Malesani, D. B., Fynbo, J. P. U., de Ugarte Postigo, A., et al. 2021, GRB Coordinates Network, 31221, 1

Mei, A., et al. 2022, arXiv:2205.08566

Most, E. R., Weih, L. R., Rezzolla, L., & Schaffner-Bielich, J. 2018, Phys. Rev. Lett., 120, 261103

Nicholl, M., Margalit, B., Schmidt, P., et al. 2021, Mon. Not. Roy. Astron. Soc., 505, 3016

Nicuesa Guelbenzu, A., Klose, S., Greiner, J., et al. 2012, A&A, 548, A101

Osborne, J. P., Page, K. L., Ambrosi, E., et al. 2021, GRB Coordinates Network, 31212, 1

Pang, P. T. H., et al. 2022, arXiv:2205.08513

Qian, Y. Z., & Woosley, S. E. 1996, Astrophys. J., 471, 331

Radice, D., Perego, A., Zappa, F., & Bernuzzi, S. 2018, Astrophys. J. Lett., 852, L29

Rastinejad, J. C., Gompertz, B. P., Levan, A. J., et al. 2022, arXiv e-prints, arXiv:2204.10864

Rossi, A., et al. 2022, Astrophys. J., 932, 1

Roth, N., & Kasen, D. 2015, Astrophys. J. Suppl., 217, 9

Rowlinson, A., Wiersema, K., Levan, A. J., et al. 2010, MNRAS, 408, 383

Ruiz, M., Shapiro, S. L., & Tsokaros, A. 2018, Phys. Rev. D, 97, 021501

Ryan, G., van Eerten, H., Piro, L., & Troja, E. 2020, Astrophys. J., 896, 166

Schlafly, E. F., & Finkbeiner, D. P. 2011, ApJ, 737, 103

Stamatikos, M., Barthelmy, S. D., D'Ai, A., et al. 2021, GRB Coordinates Network, 31209, 1

Stanek, K. Z., Matheson, T., Garnavich, P. M., et al. 2003, The Astrophysical Journal, 591, L17. https://doi.org/10.1086/376976

Stratta, G., D'Avanzo, P., Piranomonte, S., et al. 2007, A&A, 474, 827

Suvorov, A. G., Kuan, H.-J., & Kokkotas, K. D. 2022, arXiv e-prints, arXiv:2205.11112

Tanvir, N. R., Levan, A. J., Fruchter, A. S., et al. 2013, Nature, 500, 547

Tanvir, N. R., Levan, A. J., Fruchter, A. S., et al. 2015, GRB Coordinates Network, Circular Service, No. 18100, #1 (2015), 18100

Troja, E., Ryan, G., Piro, L., et al. 2018, ArXiv e-prints, arXiv:1806.10624

Troja, E., et al. 2022, Nature, 612, 228

van Eerten, H., Zhang, W., & MacFadyen, A. 2010, Astrophys. J., 722, 235

Watson, D., et al. 2019, Nature, 574, 497

Waxman, E., Ofek, E. O., & Kushnir, D. 2022, arXiv:2206.10710

Xiao, S., Zhang, Y.-Q., Zhu, Z.-P., et al. 2022, arXiv e-prints, arXiv:2205.02186

Yang, B., Jin, Z.-P., Li, X., et al. 2015, Nature Communications, 6, 7323

Yang, J., Zhang, B. B., Ai, S. K., et al. 2022, arXiv e-prints, arXiv:2204.12771

Ye, C., & Fishbach, M. 2022, arXiv:2202.05164

Zhang, B., Zhang, B.-B., Liang, E.-W., et al. 2007, The Astrophysical Journal Letters, 655, L25. http://stacks.iop.org/1538-4357/655/i=1/a=L25

Zhang, B. B., et al. 2021, Nature Astron., 5, 911

Zhang, H.-M., Huang, Y.-Y., Zheng, J.-H., Liu, R.-Y., & Wang, X.-Y. 2022, arXiv:2205.09675

Zhang, Y. Q., Xiong, S. L., Li, X. B., et al. 2021, GRB Coordinates Network, 31236, 1

Özel, F., Psaltis, D., Narayan, R., & McClintock, J. E. 2010, The Astrophysical Journal, 725, 1918

APPENDIX

A. OBSERVATIONAL DATA SELECTION

MJD [days]	Filter	Telescope/Instrument	Transient [AB mag]	Reference
u-band				
0.04 ± 0.005	u	UVOT	19.7 ± 0.2	(Rastinejad et al. 2022)
0.06 ± 0.01	u	UVOT	19.4 ± 0.2	(Rastinejad et al. 2022)
0.19 ± 0.01	u	UVOT	19.8 ± 0.1	(Rastinejad et al. 2022)
0.66 ± 0.01	u	UVOT	> 20.3	(Rastinejad et al. 2022)
0.86 ± 0.01	u	UVOT	> 20.9	(Rastinejad et al. 2022)
1.19 ± 0.01	u	UVOT	> 21.9	(Rastinejad et al. 2022)
g-band				
0.260 ± 0.081	g'	MITSuME	20.3 ± 0.2	(Ito et al. 2021)
0.69 ± 0.01	g	NOT	21.0 ± 0.04	(Rastinejad et al. 2022)
r-band				
0.431 ± 0.020	r	NEXT	20.25 ± 0.1	(Jiang et al. 2021)
0.69 ± 0.01	r	NOT	20.81 ± 0.05	(Rastinejad et al. 2022)
1.425 ± 0.001	r'	GIT	> 21.15	(Kumar et al. 2021)
i-band				
0.68 ± 0.016	i	CAHA-CAFOS	20.75 ± 0.08	(Rastinejad et al. 2022)
0.70 ± 0.01	i	NOT	20.9 ± 0.1	(Rastinejad et al. 2022)
1.68 ± 0.01	i	CAHA-CAFOS	22.6 ± 0.15	(Rastinejad et al. 2022)
5.11 ± < 0.01	i	Gemini-GMOS	26.03 ± 0.3	(Rastinejad et al. 2022)
6.08 ± < 0.01	i	Gemini-GMOS	> 25.49	(Rastinejad et al. 2022)
J-band				
0.445 ± 0.024	z	NEXT	19.9 ± 0.3	(Jiang et al. 2021)
4.72 ± 0.02	H	TNG	> 21.9	(D'Avanzo et al. 2021)
5.96 ± 0.014	J	MMT-MMRIS	24.17 ± 0.35	(Rastinejad et al. 2022)
K-band				
4.058 ± 0.005	K	Gemini-NIRI	22.41 ± 0.14	(Rastinejad et al. 2022)
5.10 ± 0.005	K	Gemini-NIRI	22.4 ± 0.2	(Rastinejad et al. 2022)
6.94 ± 0.02	K	MMT-MMRIS	23.4 ± 0.3	(Rastinejad et al. 2022)
7.98 ± 0.01	K	MMT-MMRIS	23.8 ± 0.3	(Rastinejad et al. 2022)

Table 2. Multi-wavelength observations of the counterpart and the host galaxy of GRB 211211A. Magnitudes are corrected for foreground Galactic extinction according to AV = 0.048 mag (Rastinejad et al. 2022).

B. INFERENCE SETTINGS

All parameter estimation runs were performed using the nuclear physics and multi-messenger astronomy framework NMMA (Pang et al. 2022). In this framework, joint Bayesian inferences of electromagnetic signals are carried out on the basis of the nested sampling algorithm implemented in PYMULTINEST (Buchner et al. (2014)). Each simulation used 2048 live points, and the prior settings for each of the employed models, as well as the median values and 90% credible ranges, are provided in Table 3.
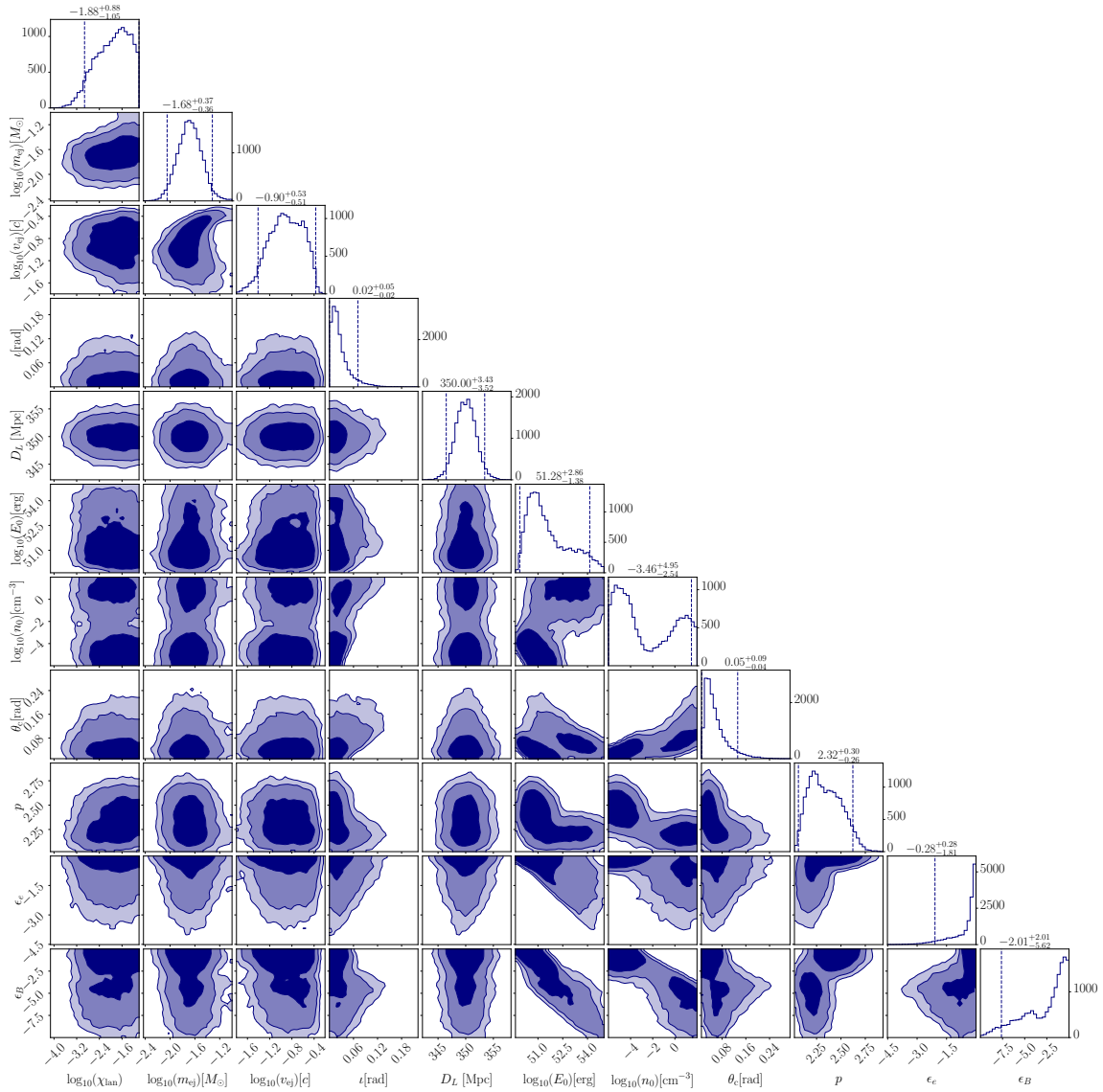
Parameter	Prior	Posterior				
		BNS-GRB$_{\rm top}^{\rm Bulla}$	BNS-GRB$_{\rm top}^{\rm Kasen}$	NSBH-GRB$_{\rm top}$	SNCol-GRB$_{\rm top}$	SN98bw-GRB$_{\rm top}$
GRB-M						
$\log_{10}(E_{\rm K,iso})$ [erg]	[47, 55]	$52.36^{+2.14}_{-2.15}$	$51.28^{+2.86}_{-1.38}$	$51.77^{+2.79}_{-1.67}$	$51.80^{+2.21}_{-1.56}$	$50.45^{+1.08}_{-0.73}$
$\theta_{\rm Obs}$ [rad]	$[0, \frac{\pi}{4}]$	$0.02^{+0.05}_{-0.02}$	$0.02^{+0.05}_{-0.02}$	$0.02^{+0.05}_{-0.02}$	$0.07^{+0.07}_{-0.06}$	$0.07^{+0.14}_{-0.05}$
θ_c [rad]	$[0.01, \frac{\pi}{10}]$	$0.05^{+0.08}_{-0.04}$	$0.05^{+0.09}_{-0.04}$	$0.05^{+0.08}_{-0.04}$	$0.09^{+0.10}_{-0.06}$	$0.10^{+0.14}_{-0.07}$
$\log_{10}(n)$ [cm^{-3}]	[-6, 2]	$-0.39^{+2.38}_{-4.78}$	$-3.46^{+4.95}_{-2.54}$	$-1.45^{+3.41}_{-4.09}$	$1.08^{+0.92}_{-3.36}$	$-4.62^{+1.41}_{-1.37}$
p	[2.01, 3]	$2.19^{+0.25}_{-0.15}$	$2.32^{+0.30}_{-0.26}$	$2.27^{+0.31}_{-0.21}$	$2.20^{+0.19}_{-0.16}$	$2.53^{+0.25}_{-0.24}$
$\log_{10}(\epsilon_e)$	[-5, 0]	$-0.80^{+0.80}_{-1.88}$	$-0.28^{+0.28}_{-1.81}$	$-0.48^{+0.48}_{-2.05}$	$-0.63^{+0.63}_{-1.55}$	$-0.10^{+0.10}_{-0.23}$
$\log_{10}(\epsilon_B)$	[-10, 0]	$-4.44^{+4.42}_{-3.60}$	$-2.01^{+2.01}_{-5.62}$	$-3.45^{+3.45}_{-4.44}$	$-4.60^{+3.66}_{-3.52}$	$-0.68^{+0.68}_{-1.48}$
D_L[Mpc]	$\mathcal{N}(350,2)$	$350.07^{+3.42}_{-3.46}$	$350.00^{+3.43}_{-3.52}$	$350.01^{+3.46}_{-3.49}$	$350.18^{+3.60}_{-3.59}$	$349.98^{+3.68}_{-3.36}$
BNS-KN-Bulla						
$\log_{10}(M_{\rm dyn}^{\rm ej})$ [$M_\odot$]	[-3, -1]	$-1.78^{+0.70}_{-0.62}$				
$\log_{10}(M_{\rm wind}^{\rm ej})$ [$M_\odot$]	[-3, -0.5]	$-1.98^{+0.55}_{-0.57}$				
Φ [deg]	[15, 75]	$62.42^{+12.58}_{-30.08}$				
BNS-KN-Kasen						
$\log_{10}(M_{\rm ej})$ [$M_\odot$]	[-2.5, -1]		$-1.68^{+0.37}_{-0.36}$			
$\log_{10}(v_{\rm ej})$ [c]	[-1.8, -1]		$-0.90^{+0.53}_{-0.51}$			
$\log_{10}(X_{\rm lan})$	[-4.5, -1]		$-1.88^{+0.88}_{-1.05}$			
NSBH-KN-Bulla						
$\log_{10}(M_{\rm dyn}^{\rm ej})$ [$M_\odot$]	[-3, -1]			$-2.51^{+0.73}_{-0.49}$		
$\log_{10}(M_{\rm wind}^{\rm ej})$ [$M_\odot$]	[-3, -0.5]			$-2.49^{+0.67}_{-0.51}$		
SNCol						
$M_{\rm ej}$ [$M_\odot$]	[0, 0.5]				$0.06^{+0.05}_{-0.04}$	
$M_{\rm Ni}$ [$M_\odot$]	[0, 0.03]				$0.00^{+0.01}_{-0.00}$	
$v_{\rm ej}$ [c]	[0, 0.5]				$0.21^{+0.04}_{-0.04}$	
$M_{\rm rp}$ [$M_\odot$]	[0, 0.05]				$0.01^{+0.01}_{-0.01}$	
$\Psi_{\rm mix}$	[0, 0.9]				$0.73^{+0.17}_{-0.35}$	
SN98bw						
$S_{\rm max}$	[0, 60]					$32.86^{+24.45}_{-24.82}$

Table 3. Model parameters and prior bounds employed in our Bayesian inferences. We report median posterior values at 90 % credibility from simulations that were run with Top-hat jet structure and with a narrow Gaussian luminosity distance prior $\mathcal{N}(\mu,\sigma)$, with mean $\mu = 350$ Mpc and standard deviation $\sigma = 2$ Mpc. We employ a conditional prior on the inclination angle depending on the jet core opening angle, $p(\theta_{\rm Obs}|\theta_{\rm c})$, using a truncated Gaussian distribution, $\mathcal{N}_T(\mu,\sigma)$, where $\mu = 0$ and $\sigma = \theta_{\rm c}$.

C. INFERENCE RESULTS

In the following, we present the posterior distribution for our reference model GRB$_{\mathrm{top}}^{\mathrm{Kasen}}$ employing a narrow distance prior centered around 350 Mpc. Figure 6 summarizes our results. As discussed in the main text, we obtain a total ejecta mass of $10^{-1.68^{+0.37}_{-0.36}}$ M$_\odot$, which is generally consistent with previous findings in the literature and an average velocity of $10^{-0.9^{+0.53}_{-0.51}}$c. Interestingly, our analysis prefers a higher lanthanide fraction compared to the one inferred for AT2017gfo using the same kilonova models (Coughlin et al. 2018), i.e., we predict a slightly redder kilonova (similar to Rastinejad et al. (2022) who predict a larger mass of the red component, but opposite to e.g. Mei et al. (2022)).

Considering the obtained GRB posteriors, we find a double peak structure in our posteriors and a clear low n_0 - high ϵ_B - high p peak, as well as, a high n_0 - low ϵ_B - low p -peak. While this double peak structure might be caused by the small set of observational data and potential degeneracies, it could also be an indicator of the missing input physics of the employed GRB models, in particular, the emission from the reverse shock that might be important at early times and wind interstellar medium density density profile, the absence of which might be responsible for the high n_0 - low ϵ_B - low p -peak.

Figure 6. Corner plot for BNS-GRB$_{\mathrm{top}}^{\mathrm{Kasen}}$ with a narrow Gaussian luminosity distance prior centered around 350 Mpc, in which we show the inferred parameters at 68%, 95%, and 99% confidence (shadings from light to dark). For the 1D posterior probability distributions, we report the median values and show the 90% confidence intervals as dashed lines.